Quantifying the effects of antibiotic treatment on the extracellular polymer network of antimicrobial resistant and sensitive biofilms using multiple particle tracking.

Lydia C. Powell,[a,b*#] Muthanna Abdulkarim,[c#] Joana Stokniene,[a] Qiu E. Yang,[d] Timothy R. Walsh[d], Katja E. Hill,[a] Mark Gumbleton,[c] David W. Thomas[a]

[a]Advanced Therapies Group, Cardiff University School of Dentistry, Cardiff, UK

[b]Centre of Nanohealth, Swansea University Medical School, Swansea University, UK.

[c]School of Pharmacy and Pharmaceutical Sciences, Cardiff University, Cardiff, UK.

[d]Medical Microbiology and Infectious Disease, School of Medicine, Cardiff University, Cardiff, UK.

*Address Correspondence to either Lydia Powell, Centre of Nanohealth, Swansea University Medical School, Swansea University, UK. Email: l.c.powell@swansea.ac.uk, or Muthanna Abdulkarim, School of Pharmacy and Pharmaceutical Sciences, Cardiff University, Cardiff, UK. Email. AbdulkarimMF@cardiff.ac.uk.

#L.C.P. and M.A. are co-first authors.

ABSTRACT

Novel therapeutics designed to target the polymeric matrix of biofilms require innovative techniques to accurately assess their efficacy. Here, multiple particle tracking (MPT) was developed to characterize the physical and mechanical properties of antimicrobial resistant (AMR) bacterial biofilms and to quantify the effects of antibiotic treatment. Studies employed nanoparticles (NPs) of varying charge and size (40-500 nm) in *Pseudomonas aeruginosa* PAO1 and methicillin resistant *Staphylococcus aureus* (MRSA) biofilms and also in polymyxin B (PMB) treated *Escherichia coli* biofilms of PMB-sensitive (PMB^{Sens}) IR57 and PMB-resistant (PMB^{R}) PN47 strains. NP size-dependent and strain-related differences in the diffusion coefficient values of biofilms were evident between PAO1 and MRSA. Dose-dependent treatment effects induced by PMB in PMB^{Sens} *E. coli* biofilms included increases in diffusion and creep compliance ($P < 0.05$), not evident in PMB treatment of PMB^{R} *E. coli* biofilms. Our results highlight the ability of MPT to quantify the diffusion and mechanical effects of antibiotic therapies within the AMR biofilm matrix; offering a valuable tool for the pre-clinical screening of anti-biofilm therapies.

KEYWORDS: multiple particle tracking, biofilm, microrheology, *mcr-1*, polymyxins

INTRODUCTION

The important role of bacterial biofilms in chronic human disease, such as cystic fibrosis, otitis media, chronic skin wounds and implant- and catheter-associated infections, has been increasingly recognized[1]. Within these biofilms, the bacteria are embedded in a complex, charged, self-produced extracellular polymeric matrix (EPS). The EPS matrix is an entangled polymer network[2] predominately composed of polysaccharides, extracellular DNA (eDNA), proteins and lipids, which facilitates biofilm formation and maturation[3]. The matrix confers considerable fitness advantages over planktonic bacteria in hydration, protection from environmental tensile or shear forces, increased cell-cell communication and enhanced horizontal gene transfer[4]. The EPS matrix also offers protection from antimicrobials, as bacteria within biofilm structures can resist conventional antibiotic therapies up to 10^3-fold[5-7]. This inherent ability of biofilms to resist antibiotics occurs through reduced metabolic activity, development of persister cells[8] and reduced antibiotic/ small molecular diffusion through the EPS polymeric network via charge-interactions[9-11].

The global rise of antibiotic resistance is an increasing problem, threatening the ability of healthcare providers to treat common bacterial infections, such as hospital-acquired methicillin-resistant *Staphylococcus aureus* (MRSA)[12]. Multidrug resistance in bacteria is also of increasing concern due to their ability to acquire multiple resistance mechanisms through horizontal gene transfer. More worrying still is the emergence of resistance to the so called 'antibiotics of last resort;' i.e. the polypeptide polymyxin antibiotics[13, 14], particularly those carried on mobile genetic elements such as plasmids. The colistin resistant *mcr-1* gene is most often isolated in *E. coli*[15, 16], although recently it

has also been found to have spread to *Klebsiella* sp. carried on a broad host range, self-transferable IncP plasmid[17] suggesting the high likelihood of imminent further spread to other Gram-negative species.

Modification of biofilm assembly and targeted disruption of the cross-linked network of "entangled polymers" within the biofilm EPS matrix would be advantageous in both clinical and industrial applications, especially with the global rise of antibiotic resistance. Most strategies fall into one of two categories; biofilm disruption or biofilm prevention. To date, anti-biofilm strategies have amongst others, included surface/substrate modification (to modify initial bacterial adhesion)[18]; disruption of the biofilm matrix using conventional antibiotics[19]; antimicrobial peptides[20]; dispersal agents[21]; detergents[22]; chelators (e.g. EDTA)[23]; EPS synthesis inhibitors[24] and dysregulation of quorum sensing within biofilms[25, 26]. In attempting to design and deliver new antimicrobial and anti-biofilm therapies, the ability to accurately measure the effects of such potential therapies upon the biofilm and biofilm matrix, and accurately quantify the complexity and variability of these biofilms is currently challenging. Conventional biofilm characterization techniques include scanning electron microscopy (SEM) and confocal laser scanning microscopy (CLSM), often combined with image analysis. These techniques however, fail to accurately characterize the EPS structure of treated biofilms, due to extensive sample preparation and/or sample dehydration, or the lack of universal dyes for EPS staining[27]. Moreover, the EPS biofilm matrix varies depending on species, strain and growth environment, for example *P. aeruginosa* produces different types of polysaccharides with varying charge namely, cationic Pel and neutral Psl, as well as anionic alginate[28-30] which further complicates characterization.

To understand the key 'fitness' advantages that biofilms possess against antimicrobial treatment, workers have sought to characterize the diffusion and material properties of the whole biofilm matrix using mesoscale and nanoscale technologies, without the need to visualize the actual EPS matrix itself. Such technologies include shear and extensional rheology[31, 32], fluorescence correlation spectroscopy (FCS)[33, 34] and fluorescence recovery after photobleaching (FRAP)[35]. Both FCS and FRAP employ fluorescently-labeled particles which can be traced within the biofilm structures. In FRAP, an area of biofilm is photo-bleached and fluorescence recovery (into the area) is modelled to determine diffusion parameters, whereas FCS is based on diffusion measurements from single-molecule fluorescence intensity fluctuations within a discrete region of the biofilm[34, 36].

Multiple particle tracking (MPT) is a recently described technique, allowing simultaneous tracking of nano-sized particles using fluorescent microscopy, from which the diffusion-based parameters of embedded particles within the EPS of bacterial biofilms can be determined[37]. MPT also facilitates measurement of the micro-rheological properties of biofilms[38]. MPT, when used in conjunction with nanoparticles (NPs) of discrete size and charge, represents a non-invasive technique which can be readily employed *in situ* within biofilms. MPT has subsequently been employed to characterize the diffusion properties of NPs within biofilms of a range of bacterial species including *P. aeruginosa*, *E. coli*, *P. fluorescens* and *S. aureus* and also to determine time-dependent changes in the biofilm matrix following adhesion[36, 37, 39, 40].

In this study, we sought to develop the MPT biofilm model to detect variations in the biofilm structure of Gram-negative *P. aeruginosa* and Gram-positive *S. aureus*

115 biofilms and examine its sensitivity and correlation to CLSM imaging. Using polymyxin
116 B sensitive (PMB^{Sens}) and resistant (PMB^{R}) *E. coli* strains, we examined the sensitivity of
117 the MPT biofilm model to detect variations in the biofilm structure after dose-dependent
118 polymyxin B antibiotic therapy in comparison to traditional confocal microscopy. By
119 using commercially available NPs, this study highlights the usefulness and sensitivity of
120 the MPT technique in the development of novel anti-biofilm therapeutics for AMR
121 infections.
122
123 **RESULTS**
124 CLSM imaging and MPT measurements identify distinct variations in *S. aureus* and *P.*
125 *aeruginosa* biofilms
126 CLSM imaging of *S. aureus* 1004A (MRSA) and *P. aeruginosa* PAO1 revealed variation
127 in the structural properties of the biofilms produced by the two strains. While MRSA
128 formed a thin, but bacterially-dense biofilm structure, PAO1 biofilms possessed greater
129 height, but appeared less bacterially-dense (Supplementary Fig. 1). These CLSM images
130 correlated well with diffusion of the negatively-charged NPs (40–500 nm) through the
131 biofilm, with NP diffusion being lower in the MRSA biofilms when compared to those of
132 PAO1 (40 and 200 nm NPs; $P < 0.01$). In contrast, diffusion of the positively-charged
133 NPs (200 nm) in both biofilms were similar ($P > 0.05$; Table 1).
134 MPT revealed that as the size of the negatively-charged particles increased, the
135 diffusion coefficient of the particles within PAO1 biofilms decreased significantly (40-
136 200 nm; $P < 0.05$). This significant trend was also evident in the MRSA biofilms for
137 particle sizes of 40-200 nm. Also, while diffusion of the positively charged 200 nm NPs

138 in PAO1 biofilms was significantly reduced when compared with the diffusion of the
139 negatively-charged NPs of the same size ($P < 0.05$), in MRSA biofilms, the diffusion of
140 the positively-charged NPs was not significantly different when compared to the
141 negatively-charged particles ($P > 0.05$; Table 1).

142 The ratio of the biofilm diffusion coefficient to the diffusion coefficient in water
143 ($\langle Deff \rangle / D^o$) allows measurement of NP diffusion through the biofilm structure in relation
144 to the intrinsic free Brownian motion of the NPs in water, thereby taking into account the
145 impact of NP size on its unrestricted diffusion in liquid. The percentage ratio of
146 $\langle Deff \rangle / D^o$ revealed that the diffusion of 200 and 500 nm sized NPs were significantly
147 lower than diffusion of 40 and 100 nm NPs in both MRSA and PAO1 biofilms ($P <$
148 0.05). However, negatively-charged NP diffusion was still greater (by at least 2.5 times)
149 in PAO1 biofilms when compared to their diffusion in MRSA biofilms (Table 1).

150 PAO1 biofilms displayed greater heterogeneity in negatively-charged NP movement
151 with resultant $90^{th}/10^{th}$ percentile ratios of 100-987, when compared to MRSA biofilms
152 which displayed much lower ratios of 3-85 (Fig. 1). The heterogeneity data again
153 confirmed the observed variations in the structural properties between the MRSA and
154 PAO1 biofilms seen in the CLSM images. The data also revealed that there was
155 increasing heterogeneity in NP diffusion with increasing particle size until the NP size
156 reached 100 nm for *S. aureus* and 200 nm for *P. aeruginosa* biofilm systems, after which
157 heterogeneity in NP diffusion then decreased.

158 The exponential anomalous values of both PAO1 and MRSA biofilms calculated
159 using 40-500 nm NPs appeared to demonstrate a viscous response of these biofilms ($\alpha >$
160 0.5; Fig. 2).

161

162 CLSM and MPT measurements describe dose-dependent disruption of *E. coli* IR47

163 biofilms treated with polymyxin B

164 MIC assays of PMB^{Sens} *E. coli* IR57 and PMB^{R} *E. coli* PN47 were performed to confirm

165 strain sensitivity to the antibiotic, giving MIC values against polymyxin B of 0.06 and 2

166 µg/ml respectively.

167 The CLSM assay revealed cellular aggregation and disruption of the PMB^{Sens} *E. coli*

168 IR57 biofilm matrix in a dose-dependent manner following polymyxin B treatment (Fig.

169 3a). This finding was confirmed by MPT through dose-dependent increases in the

170 effective diffusion coefficients (<Deff>) within the treated biofilms for all three NP sizes

171 tested (100, 200 and 500 nm; Fig. 3), with the 100 nm NPs revealing the greatest dose-

172 dependent sensitivity in diffusion coefficients to antibiotic treatment. The dose-

173 dependent changes in NP diffusion coefficients, starting from 2 µg/ml polymyxin B

174 treatment, were all significantly different from the control ($P < 0.05$).

175 Polymyxin B treatment (2-8 µg/ml) revealed a greater increase in the mean square

176 displacement <MSD> versus time measurements for the 200 and 500 nm particles when

177 compared to the 100 nm particles, indicative of increasing pore size within the biofilm

178 structure following polymyxin B treatment (Fig. 4). The exponential anomalous values

179 of the *E. coli* biofilms demonstrated that polymyxin B treatment had little effect on the

180 viscoelastic response of the biofilms (Fig. 4). However, the dose–dependent disruption of

181 the *E. coli* IR57 biofilms was reflected in increasing biofilm creep compliance (J(t)) with

182 increasing polymyxin B dose, observed with all 3 NP sizes tested (Fig. 5).

183

MPT measurements describe distinct variations in the response of PMB^{Sens} *E. coli* IR47 and PMB^{R} *E. coli* PN47 biofilms to polymyxin B treatment

To assess the impact of resistance to polymyxin B on treatment of *E. coli* biofilms, two strains of *E. coli* (PMB^{R} PN47 and PMB^{Sens} IR45) were selected based on their susceptibility to polymyxin B. The MPT assay revealed that the diffusion coefficients <Deff> of 200 nm NPs was greatly increased in the PMB^{Sens} IR45 biofilms (0.0643 vs. 0.34 cm^2. s^{-1} x 10^{-9}) following treatment, while NP diffusion within the PMB^{R} PN47 biofilms remained largely unchanged (Table 2). This trend was reflected in the heterogeneity of the NP diffusion measurements (Fig. 6), where the PMB^{Sens} IR45 demonstrated decreased $90^{th}/10^{th}$ percentile ratio of 2577 to 198 following treatment, revealing more homogenous NP diffusion, indicative of increasing biofilm pore size with antibiotic treatment. As before, the heterogeneity of the NP diffusion measurements within the PMB^{R} PN47 biofilms demonstrated little response to treatment. This result was also confirmed by the creep compliance data showing increasing values following polymyxin-B treatment in the PMB^{Sens} strain, but not in the PMB^{R} strain (Fig. 7). Interestingly, NP diffusion (<Deff>) for the PMB^{Sens} IR45 was more than 3 times greater than <Deff> for PMB^{R} PN47 (Table 2). NP diffusion within the PMB^{Sens} strain appeared to be vastly more heterogeneous than for the PMB^{R} strain, indicating that pore size was more heterogeneous in the biofilms of the PMB^{Sens}strain (Fig. 6).

DISCUSSION

NPs are being increasingly applied in a variety of medical applications, such as in the diagnosis and treatment of human disease (e.g. drug- and gene delivery)[41] and as novel

research tools (both *in vitro* and *in vivo*) to improve our understanding of biological systems and human illness[42-44]. This study has demonstrated the use of MPT with traceable NPs as a robust, non-invasive, *in situ* technique to inform our understanding of biofilms and further our insight into the potential effects of antimicrobial and anti-biofilm therapies on the biofilm matrix, and on biofilm-related changes induced with the acquisition of antibiotic resistance.

The EPS matrix of biofilms varies not only between species and strains, but also with differences in environmental growth conditions, such as surface composition/roughness, nutrient availability, temperature, and hydrodynamic shear[38, 45]. As a result, the net charge and functional groups present within the matrix, as well as biofilm pore size exhibit considerable variations. To assess variations in biofilm structure between bacterial species, the diffusion coefficients of fluorescently-labelled NPs were initially measured in both Gram-positive *S. aureus* 1004A (MRSA) and Gram-negative *P. aeruginosa* PAO1, revealing the influence of both NP size and surface-charge on diffusion through the respective biofilm structures. The influence of NP charge was clearly evident in the diffusion coefficient measurements of 200 nm NPs within *P. aeruginosa* PAO1 biofilms, with reduced diffusion of amine-modified (positively-charged) particles compared to the carboxylated (negatively-charged) NPs. In *P. aeruginosa* PAO1, the exopolysaccharides form a major part of the EPS matrix and are composed of negatively-charged alginate, neutrally-charged Psl and positively-charged Pel, while eDNA in biofilm matrixes has been shown to be negatively-charged[46]. Our results indicate a net negative charge of the *P. aeruginosa* EPS matrix, where the existence of increased negative charges within the EPS matrix reduced the diffusion

coefficient of the positively-charged amine-modified NPs. In *S. aureus* MRSA biofilms, whilst the diffusion coefficient of the amine-modified NPs was twice that of the carboxylated-modified NPs, these values were not significantly different. In *S. aureus,* the two major components of EPS matrix are the positively-charged poly-N-acetylgluosamine (PNAG) polysaccharides and negatively-charged eDNA[47, 48]. These results potentially indicate a net positive charge of the MRSA EPS matrix; increased positive charges within the matrix reducing the diffusion coefficient of the negatively-charged carboxylated NPs. However, as the diffusion coefficient values achieved with 200 nm carboxylated NPs were similar to those observed with 500 nm NPs in MRSA (0.0031 vs 0.0038 cm^2 S^{-1} $x10^{-9}$ respectively), this indicated the inability of the 200 nm NPs to freely move within the dense MRSA biofilm matrix. The restricted movement of 200 nm NPs within the MRSA biofilms resulted in small, distinct differences in diffusion coefficient between the amine-modified NPs and carboxylated-modified NPs, which may have been more pronounced with the use of smaller sized amine-modified NPs.

In this model, NP diffusion into the biofilm EPS matrix was not only clearly influenced by charge, but also by their size[49-51]. Large particles may not be able to permeate into the biofilm EPS structure due to steric hindrance or biofilm pore size, while hydrophobic/electrostatic interactions may influence the diffusion of smaller particles[38]. Previous researchers have used a variety of techniques to characterise the internal structure and pore size of biofilms. Zhang et al[52] originally employed sectioning by microtome and dye adsorption to describe the heterogeneity in pore size within wastewater biofilms, where biofilm pore sizes ranged between 0.3-2.7 μm. More recently, Rosenthal et al (2018)[53] used optical coherence tomography (OCT) to

253 characterize the heterogeneous network of a thick, multi-species biofilm, where pore
254 diameters as large as 110 μm were measured, while other researchers have demonstrated
255 pore size ranges of 500-1000 nm[54] and >100 nm[55] using single-particle tracking
256 techniques.

257 In the current study, the effect of NP size on diffusion was clearly evident in PAO1
258 and MRSA biofilms, where a reduction in NP size (< 200 nm), induced a dramatic rise in
259 particle diffusion; a finding possibly indicative of a mean biofilm pore size < 200 nm.
260 Similarly, Peulen and Wilkinson[56] demonstrated increasing diffusion coefficients with
261 decreasing size and negative charge of silver NPs in *Pseudomonas fluorescens* biofilms,
262 where the optimum particle size for diffusion in these dense biofilms was < 50 nm. The
263 increased NP diffusion coefficients in PAO1 biofilms when compared to the MRSA
264 biofilms (40-500 nm carboxylated-modified NPs) was evident in this study and reflected
265 the biofilm architecture; CLSM imaging demonstrating the more dense structure of the
266 MRSA biofilms.

267 Profiling of the diffusion coefficients of 360 individual particles through ranking
268 <Deff> data into percentiles (highest 90th to lowest 10th percentiles) provides insight
269 into the heterogeneity of particle movement, which may be indicative of heterogeneous
270 pore sizes within the biofilm itself[57, 58]. This study revealed that NP diffusion coefficients
271 became more heterogeneous with increasing particle size until a NP size of 100 nm for *S.*
272 *aureus* and 200 nm for *P. aeruginosa* biofilms was reached, at which point NP diffusion
273 became more homogeneous (the particle size becoming too large to facilitate free
274 movement within the biofilm structure) with NP movement occurring only through larger
275 pore sizes. This data demonstrates contrasting inter-species biofilm architecture; *P.*

aeruginosa forming a pore structure that was larger in size and more heterogeneous compared to that of *S. aureus* biofilms.

MPT may, in the future, offer valuable insight in characterizing the EPS matrix of heterogeneous polymicrobial biofilms which are commonly found in human disease states[59, 60]. Whilst these biofilms are heterogeneous, they are often composed of distinct, individual 'pockets' of homogenous single-species growth and MPT coupled with GFP-labelled bacterial populations or Fluorescence in situ hybridization (FISH) labelling may be employed to visualize and analyse the biofilm matrix of these bacterial populations.

Structurally, biofilms possess a complex architecture, being composed of cell clusters surrounded by voids and water channels[61]. Biofilm structures possess viscoelastic properties (exhibiting both elastic and viscous properties) which can aid biofilm survival under mechanical and chemical loads[62, 63]. Cao et al[37] employed single particle tracking with CLSM imaging to characterize the viscoelastic properties of cell clusters and voids within *P. fluorescens* biofilms, demonstrating that the viscoelastic properties (creep compliance) of the 'biofilm void' zones was the primary contributor to the viscoelastic properties of the biofilm. Importantly, whilst the larger (500 nm) NPs employed in this study were unable to diffuse into the bacterial cell clusters, their diffusion into the biofilm voids could still provide a sensitive and reproducible model to monitor changes in the viscoelastic properties of biofilms. In this study, calculation of the exponential anomalous values revealed that PAO1 and MRSA biofilms displayed viscous behavior when assessed using 40 – 500 nm NPs however, no micro-rheological differences could be determined between the well-established 72 h grown PAO1 and MRSA biofilms.

299 The resistance of bacterial biofilms to antibiotic therapy has been widely reported in
300 the literature, with high levels of antibiotic tolerance arising due to a number of different
301 factors[64]. Penetration of antibiotics through the biofilm EPS matrix can vary
302 considerably depending on how they interact with the charged components of the EPS[10,
303 11]. Previous research has shown that cationic antibiotics (e.g. tobramycin) exhibit charge-
304 mediated binding to polyanions within the biofilm EPS matrix, resulting in reduced
305 penetration of antibiotics into the biofilm structure[9, 65]. Sankaran et al[34], however,
306 demonstrated that both labelled aminoglycoside tobramycin (positively-charged) and the
307 fluoroquinolone ciprofloxacin (neutrally-charged) were able to diffuse into, and remained
308 mobile within the interior of *P. aeruginosa* biofilms, demonstrating that reduced
309 antibiotic diffusion in the EPS matrix is not solely responsible for the antibiotic tolerance
310 of biofilms[66]. Moreover, the development of a sub-population of persister cells (with low
311 or dormant metabolic activity) may ensure that a small cohort of cells within the biofilm
312 can withstand multiple doses of antimicrobial therapy[67]. Expression of biofilm-specific
313 genetic mechanisms may also occur[11], making the biofilm less susceptible to
314 antimicrobial attack.
315 Zrelli et al[68] and Reighard et al[39] demonstrated the failure of antibiotic treatment
316 (afloxacin, ticarcillin, tobramycin) to induce changes in the NP diffusion and mechanical
317 properties of *E. coli* and *P. aeruginosa* biofilms using particle tracking methodologies. In
318 contrast, here we demonstrate the dose-dependent disruption of the PMB^{sens} *E. coli*
319 biofilm matrix induced by exposure to polymyxin B, with significant increases in NP
320 diffusion and creep compliance in the treated biofilms. Klinger-Strobel et al[69]
321 demonstrated the ability of colistin (polymyxin E) to disrupt 48 h *E. coli* biofilms at

concentrations of 4-16 µg/ml (with MICs ranging from 1 to 0.0625 µg/ml for laboratory strains and clinical isolates respectively). The authors suggested that colistin destabilized the biofilm matrix (even in strains with intrinsic polymyxin resistance) leading to the dispersal of planktonic cells that were then more susceptible to antibiotics. The published, susceptibility breakpoints for polymyxins are S ≤2 µg/ml > R for *E. coli* (EuCAST 2018)[70]. The concentrations of polymyxin B used in our study were relatively high (2 to 64 µg/ml), equal to, or above, the MIC values (0.06 to 2 µg/ml), to induce effective disruption of the biofilm structure. However, differences in NP diffusion were detected at lower concentrations (2 µg/ml) than that employed by Klinger-Strobel et al[69].

Witten and Ribbeck[38] proposed that biofilm permeability may be a biomarker for antimicrobial resistance, and the data here demonstrates the sensitivity of the MPT biofilm assay in this respect. In the PMB^{sens} *E. coli* IR57 (MIC 0.06 µg/ml) biofilms, MPT was able to detect structural, pore-size related changes induced within the biofilm matrix with antibiotic dosing as low as 2 µg/ml (a clinically-relevant concentration) where changes in the treated biofilm structure were indiscernible at this concentration using conventional CLSM imaging. The disruptive effect of polymyxin B on the *E. coli* biofilm structure was however, evident in CLSM imaging at higher concentrations (> 32 µg/ml). We also sought to model biofilm disruption by polymyxin B in PMB^{R} *E. coli* as we have previously demonstrated that *mcr-1* and *-3* expression in *E. coli* is associated with alterations in bacterial viability within the biofilm matrix[16, 71], hypothesizing that the acquisition of polymyxin resistant *mcr-1* was an evolutionary 'trade-off'; resistance to polymyxin being associated with decreased biofilm biomass and growth in 24 h biofilm formation assays[71]. Here we clearly demonstrate resistance to biofilm disruption of

345 PMB^R PN47 following treatment with polymyxin B (8 µg/ml) in well-established 72 h
346 grown biofilms.

347 The observed variations in particle diffusion and creep compliance with
348 antibiotic/antimicrobial treatment in this study could also be crucial in understanding the
349 interaction of the innate immune system with biofilm infections. Increased pore size and
350 decreased mechanical properties of the biofilm structure may facilitate increased
351 inflammatory cell penetration into the biofilm matrix, thereby improving bacterial
352 clearance[72]. Moreover, increased porosity of biofilm structures may allow greater
353 penetration of antimicrobial agents and may be of benefit, especially in treating implant
354 biofilm-related infections[73].

355 This study demonstrated not only the ability of MPT to detect disruption in biofilm
356 structures, but also revealed the ability of the technique to dissect the effects of
357 antimicrobial and anti-biofilm therapies, not always discernible using conventional
358 technologies. Here, the ability of MPT to inform understanding of, and test therapies
359 against, emergent antimicrobial resistant pathogens is clear. As anti-biofilm therapies
360 play a clear role in increasing susceptibility of resistant bacteria to existing therapies, the
361 utility of MPT in assessing novel therapies to disrupt the biofilm matrix e.g. chelating
362 agents[23] and G-block alginate oligomers[31, 74] may be invaluable in the future. MPT may
363 further our insight into the potential effects of such antimicrobial therapies *in vivo* and
364 provide increased understanding into the biofilm matrix and biofilm-related changes
365 induced with the acquisition of antibiotic resistance.

366

367 **MATERIALS AND METHODS**

368 Bacterial strains, growth media and culture conditions

369 The following strains were used in this study; *Pseudomonas aeruginosa* PAO1,
370 methicillin resistant *Staphylococcus aureus* (MRSA 1004A)[75], polymyxin B-resistant
371 (PMB^R) *Escherichia coli* PN47 (carrying the colistin resistance plasmids *mcr-1* and *mcr-*
372 *3*)[76] and polymyxin B-sensitive (PMB^{Sens}) *E. coli* IR57. Bacterial colonies were sub-
373 cultured on LB agar plates supplemented with/without 2 µg/ml polymyxin B (Sigma-
374 Aldrich). Overnight bacterial cultures were grown in Tryptone Soy Broth (TSB; Oxoid)
375 for 37ºC at 120 rpm. Biofilms were grown in cation-adjusted Mueller Hinton Broth
376 (MHB; LabM) with/without supplementation with the antibiotic polymyxin B.
377
378 Minimum Inhibitory Concentration (MIC) measurements

379 Overnight bacterial cultures were adjusted to a standardized cell suspension of
380 approximately 10^8 colony forming units (CFU)/ml (equivalent to 0.5 McFarland
381 standard). Two-fold serial dilutions in polymyxin B were prepared in MHB within flat
382 bottom 96-well microtiter plates (100 µl per well). The adjusted O/N bacterial cultures
383 were then diluted 10-fold in MHB and 5 µl added to the microtiter plate containing the
384 antibiotic serial dilutions to give a final concentration of 5×10^5 CFU/ml. The plates were
385 incubated for 16 to 20 h (37ºC) and MICs determined as the lowest concentration at
386 which there was no visible growth.
387
388 Biofilm growth

389 Overnight bacterial cultures were adjusted to a standardized cell suspension of 1×10^7
390 CFU/ml in MHB. First, 0.2 ml of adjusted O/N culture was placed into the center of each

glass well within a 12-well dish (glass thickness 1.5 mm and 14 mm diameter; MatTek) and incubated statically for 1 h. Then, 1.8 ml of fresh MHB was placed into each well and incubated statically for 24 h at 37^{o}C. A further 1 ml of MHB was then placed into each well and plates incubated for a further 24 h (37^{o}C). Following 48 h growth, biofilms were treated with a further 1 ml of MHB which was added into each well with a further incubation of 24 h (37^{o}C), resulting in a total biofilm growth time of 72 h.

Polymyxin B treatment of *E. coli* biofilms

Following 48 h growth, *E. coli* biofilms were treated with either 1 ml of MHB (control) or 1 ml polymyxin B (2, 8, 16, 32, 64 µg/ml; treatment) which was added into each well with a further incubation of 24 h (37^{o}C), resulting in a total biofilm growth time of 72 h.

SYTO 9 staining and CLSM imaging of biofilms

After 72 h growth, the bacterial supernatant was carefully removed and the bacterial cells within the biofilms stained with 0.5% Syto 9® dye (Invitrogen; 400µl) for 1 h. After staining, the biofilms were washed with phosphate buffered saline (PBS; x2) prior either to CLSM Z-stack imaging using a Leica TCS SP5 CLSM or NP addition.

MPT measurement of bacterial biofilms

NPs used in this study were either negatively-charged carboxylate-modified *Fluo*spheres® (40, 100, 200 and 500 nm) or positively-charged amino-modified *Fluo*spheres® (200 nm) ([Ex/Em]: [580/605 nm]; ThermoFisher Scientific). The zeta potential and sizing values of the NPs were characterized in PBS buffer using a Malvern

414 Zetasizer Nano ZS prior to MPT studies. For MPT experiments, the *Fluo*spheres®
415 suspension was vortexed for 1 min then diluted in sterilized PBS buffer (0.0025%),
416 before addition of 10 µl diluted *Fluo*spheres® suspension onto the biofilms followed by a
417 2 h incubation. Biofilms were stained with SYTO 9® before addition of the *Fluo*spheres®
418 to visualize the lower layers of the biofilm matrix using a Leica DM IRB wide-field
419 Epifluorescence microscope (x63 oil immersion lens). Videos of particle movement
420 within the biofilms were captured at a frame rate of 33 ms (600 frames, 20 s) using a high
421 speed camera (Allied Vision Technologies, UK) and then particle trajectories were
422 tracked using ImageJ software (Mosaic) over 2 s to convert NP movements into metric
423 displacements in both the X and Y directions[43, 77]. Ensemble mean square displacement
424 ‹MSD›, effective diffusion coefficient ‹Deff›, and heterogeneity of particle diffusion were
425 measured as described in supplementary materials[57; 78]. Here, 120 particle movements
426 were captured in each biofilm well, and each bacterial strain was tested in triplicate (i.e.
427 360 particles in total for each biofilm species).
428 The viscoelastic properties of the biofilms were assessed by determining the
429 anomalous diffusion exponent (α). This was calculated by fitting the power law to
430 log(‹MSD›) versus log(Δt) and calculating the slope of this data[79], where $\alpha = 1$ for a
431 completely viscous system (liquid), $\alpha = 0$ for a completely elastic system (solid) and $1 >$
432 $\alpha > 0$ for a viscoelastic system[39, 40]. Additionally, the micro-rheological properties of the
433 biofilms were further defined by calculation of the creep compliance (J(t)), where the
434 MSD represents deformation of the biofilm within time (Δt) under constant
435 pressure/shear force represented by the temperature of the atmosphere. Creep
436 compliance (J(t)) was calculated by the following equation:

$$J(t) = \frac{3\pi d}{4k_B T}\langle MSD(t)\rangle$$

where k_B is the Boltzmann constant, T is absolute temperature and d is the diameter of the particle [80].

Statistical analysis

Statistical software (Minitab, State College, PA) was used to calculate significant differences with ANOVA testing with *post hoc* Tukey multi-comparison tests for the statistical analyses presented.

DATA AVAILABILITY

Data generated and analyzed during this study are included in this published article and its Supplemental information file. Additional details available upon reasonable request.

ACKNOWLEDGMENTS

We thank Prof. Timothy Walsh and Dr Brad Spiller for the *E.coli* PN47 strain. We thank the National Research Network for Life Sciences and Health (NRN) and MRC-Proximity to Discovery Scheme (MC-PC_17186) for funding. The funders had no role in study design, data collection and interpretation, or the decision to submit the work for publication.

COMPETING INTERESTS

The authors declare no competing interests.

AUTHOR CONTRIBUTIONS

L.C.P. and M.A. are co-first authors. Funding acquisition: D.W.T., M.G., L.C.P., M.A., K.E.H. Conceived and designed experiments: D.W.T., M.G., L.C.P., M.A. Performed the experiments: L.C.P., M.A., J.S., K.E.H. Analysed the data: M.A., L.C.P. Contributed reagents/materials/analysis tools: Q.E.Y., T.R.W. Wrote and edited the paper: L.C.P., M.A., K.E.H., M.G., D.W.T.

ADDITIONAL INFORMATION

Supplementary information is available for this paper.

REFERENCES

1. Bjarnsholt, T. The role of bacterial biofilms in chronic infections. *APMIS Suppl* **136**, 1-51 (2013).
2. Mazza, MG. The physics of biofilms- an introduction. *J Phys D Appl Phys* 49, 203001 (2016).
3. Flemming, H-C. et al. Biofilms: an emergent form of bacterial life. *Nat Rev Microbiol* **14**, 563-575 (2016).
4. Boudarel, H., Mathias, J-D., Blaysat, B. & Grediac, M. Towards standardized mechanical characterization of microbial biofilms: analysis and critical review. *NPJ Biofilms Microbiomes* **4**, 17 (2018).
5. Mah, T. F. Biofilm-specific antibiotic resistance. *Future Microbiol* **7**, 1061-1072 (2012).

6. Ceri, H. et al. The Calgary biofilm device: new technology for rapid determination of antibiotic susceptibilities of bacterial biofilms. *J Clin Microbiol* **37**, 1771-1776 (1999).
7. Moskowitz, S. M., Foster, J. M., Emerson, J. & Burns, J. L. Clinically feasible biofilm susceptibility assay for isolates of *Pseudomonas aeruginosa* from patients with cystic fibrosis. *J Clin Microbiol* **42**, 1915-1922 (2004).
8. Høiby, N., Bjarnsholt, T., Givskov, M., Molin, S. & Ciofu, O. Antibiotic resistance of bacterial biofilms. *Int J Antimicrob Agents* **35**, 322-332 (2010).
9. Tseng, B. S. et al. The extracellular matrix protects *Pseudomonas aeruginosa* biofilms by limiting the penetration of tobramycin. *Environ Microbiol* **15**, 2865–2878 (2013).
10. Hunt, B. E., Weber, A., Berger, A., Ramsey, B. & Smith, A. L. Macromolecular mechanisms of sputum inhibition of tobramycin activity. *Antimicrob Agents Chemother* **39**, 34–39 (1995).
11. Mah, T. F. et al. A genetic basis for *Pseudomonas aeruginosa* biofilm antibiotic resistance. *Nature* **426**, 306–310 (2003).
12. Lindsay, J. A. Hospital-associated MRSA and antibiotic resistance – what have we learned from genomics? *Int J Med Microbiol* **303**, 318-323 (2013).
13. Corona, A. & Cattaneo, D. Dosing colistin properly: Let's save 'Our Last Resort Old Drug. *Clin Infect Dis* **65**, 870 (2017).
14. Bulman, Z. P. et al. Polymyxin combinations combat *Escherichia coli* harboring *mcr-1* and $bla_{\text{NDM-5}}$: Preparation for a post-antibiotic era. *MBio* **8**, e00540-17 (2017).

15. Poirel, L. et al. Antimicrobial resistance in *Escherichia coli*. *Microbiol Spectr* **6**, 4 (2018).
16. Yang, Q. et al. Balancing mcr-1 expression and bacterial survival is a delicate equilibrium between essential cellular defense mechanisms. *Nat Commun* **8**, 2054 (2017).
17. Zhao, F., Feng, Y., Lü, X., Mcnally, A. & Zong, Z. IncP plasmid carrying colistin resistance gene *mcr-1* in Klebsiella pneumoniae from hospital sewage. *Antimicrob Agents Chemother* **61**, e02229-16 (2017).
18. Lemire, J. A., Harrison, J. J. & Turner, R. J. Antimicrobial activity of metals: mechanisms, molecular targets and applications. *Nat Rev Micro* **11**, 371–384 (2013).
19. Bayramov, D. F. & Neff, J. A. Beyond conventional antibiotics - New directions for combination products to combat biofilm. *Adv Drug Deliv Rev* **112**, 48-60 (2016).
20. Pletzer, D., Coleman, S. R. & Hancock, R. E. Anti-biofilm peptides as a new weapon in antimicrobial warfare. *Curr Opin Microbiol* **33**, 35-40 (2016).
21. Barraud, N., Kelso, M. J., Rice, S. A. & Kjelleberg, S. Nitric oxide: a key mediator of biofilm dispersal with applications in infectious diseases. *Curr Pharm Des* **21**, 31-42 (2015).
22. Otzen, D. E. Biosurfactants and surfactants interacting with membranes and proteins: Same but different? *BBA: Biomembranes* **1859**, 639-649 (2017).
23. Finnegan, S. & Percival. S. L. EDTA: An Antimicrobial and Antibiofilm Agent for Use in Wound Care. *Adv Wound Care* **4**, 415-421 (2015).

24. Pandit, S. et al. Low concentrations of Vitamin C reduce the synthesis of extracellular polymers and destabilize bacterial biofilms. *Front Microbiol* **8**, 2599 (2017).
25. Jack, A. A. et al. Alginate oligosaccharide-induced modification of the *lasI-lasR* and *rhlI-rhlR* quorum sensing systems in *Pseudomonas aeruginosa*. *Antimicrob Agents Chemother* **62**, e02318–17 (2018).
26. Brackman, G. & Coenye, T. Quorum sensing inhibitors as anti-biofilm agents. *Curr Pharm Des* **21**, 5-11 (2015).
27. Pan, M., Zhu, L., Chen, L., Qiu, Y. & Wang, J. Detection techniques for extracellular polymeric substances in biofilms: A review. *BioRes* **11**, 8092-8115 (2016).
28. Jennings, L. K. et al. Pel is a cationic exopolysaccharide that cross-links extracellular DNA in the *Pseudomonas aeruginosa* biofilm matrix. *Proc Natl Acad Sci USA* **112**,11353-11358 (2015).
29. Billings, N. et al. The extracellular matrix component Psl provides fast-acting antibiotic defense in *Pseudomonas aeruginosa* biofilms. *PLoS Pathog* **9**, e1003526 (2013).
30. Franklin, M. J., Nivens, D. E., Weadge, J. T. & Howell, P. L. Biosynthesis of the *Pseudomonas aeruginosa* extracellular polysaccharides, alginate, Pel, and Psl. *Front Microbiol* **167**,1–16 (2011).
31. Powell, L. C. et al. The effect of alginate oligosaccharides on the mechanical properties of Gram-negative biofilms. *Biofouling* **29**, 413-421 (2013).
32. Pritchard, M. F. et al. A low-molecular-weight alginate oligosaccharide disrupts

pseudomonal microcolony formation and enhances antibiotic effectiveness. *Antimicrob Agents Chemother* **61**, e00762-17 (2017).

33. Gulot, E. et al. Heterogeneity of diffusion inside microbial biofilms determined by fluorescence correlation spectroscopy under two-photon excitation. *Photochem Photobiol* **75**, 570-578 (2002).
34. Sankaran, J. et al. Single microcolony diffusion analysis in *Pseudomonas aeruginosa* biofilms. *NPJ Biofilms Microbiomes* **5**, 35 (2019).
35. Waharte, F., Steenkeste, K., Briandet, R. & Fontaine-Aupart, M. P. Diffusion measurements inside biofilms by image-based fluorescence recovery after photobleaching (FRAP) analysis with a commercial confocal laser scanning microscope. *Appl Environ Microbiol* **76**, 5860-5869 (2010).
36. Billings, N., Birjiniuk, A., Samad, T. S., Doyle, P. S. & Ribbeck, K. Materials properties of biofilms - a review of methods for understanding permeability and mechanics. *Rep Prog Phys* **78**, 036601 (2015).
37. Cao, H. et al. Revealing region-specific biofilm viscoelastic properties by means of a micro-rheological approach. *NPJ Biofilms Microbiomes* **2**, 5 (2016).
38. Witten, J. & Ribbeck, K. The particle in the spider's web: transport through biological hydrogels. *Nanoscale* **9**, 8080- 8095 (2017).
39. Reighard, K. P., Hill, D. B., Dixon, G. A., Worley, B. V. & Schoenfisch, M. H. Disruption and eradication of *P. aeruginosa* biofilms using nitric oxide-releasing chitosan oligosaccharides. *Biofouling* **31**, 775–787 (2015).

572 40. Chew, S. C., Rice, S. A., Kjelleberg, S. & Yang, L. In situ mapping of the
573 mechanical properties of biofilms by particle-tracking microrheology. *J Vis Exp* **4**,
574 e53093 (2015).
575 41. Zazo, H., Colino, C. I. & Lanao, J. M. Current applications of nanoparticles in
576 infectious diseases. *J Control Release* **224**, 86-102 (2016).
577 42. Natan, M. & Banin, E. From nano to micro: using nanotechnology to combat
578 microorganisms and their multidrug resistance. *FEMS Microbiol Rev* **41**, 302–322
579 (2017).
580 43. Inchaurraga, L. et al. Modulation of the fate of zein nanoparticles by their coating
581 with a Gantrez® AN-thiamine polymer conjugate. *Int J Pharm X* **1**, 100006
582 (2019).
583 44. Brotons-Canto, A. et al. Evaluation of nanoparticles as oral vehicles for
584 immunotherapy against experimental peanut allergy. *Int J Biol Macromol* **110**,
585 328–335 (2018).
586 45. Fulaz, S., Vitale, S., Quinn, L. & Casy, E. Nanoparticle-biofilm interactions: The
587 role of the EPS matrix. *Trends Microbiol* **27**, 915-926 (2019).
588 46. Jennings, L. K. et al. Pel is a cationic exopolysaccharide that cross-links
589 extracellular DNA in the *Pseudomonas aeruginosa* biofilm matrix. *PNAS*
590 **112**,11353-11358 (2015).
591 47. Dengler, V., Foulston, L., DeFrancesco, A., Losick, R. An electrostatic net model
592 for the role of extracellular DNA in biofilm formation by *Staphyloccous aureus*. *J*
593 *Bacteroil* **197**, 3779-3787 (2015).

48. Hiltunen, A. K. et al. Structural and functional dynamics of *Staphylococcus aureus* biofilms and biofilm matrix proteins on different clinical materials. *Microorganisms* **7**, 584 (2019).
49. Campoccia, D., Montanaro, L. & Arciola, C. R. A review of the biomaterials technologies for infection-resistant surfaces. *Biomaterials* **34**, 8533–8554 (2013).
50. Habimana, O., Steenkeste, K., Fontaine-Aupart, M. P., Bellon-Fontaine, M-N. & Briandet, R. Diffusion of nanoparticles in biofilms is altered by bacterial cell wall hydrophobicity. *Appl Environ Microbiol* **77**, 367–368 (2011).
51. Ikuma, K., Decho, A. W. & Lau, B. L. T. When nanoparticles meet biofilms—interactions guiding the environmental fate and accumulation of nanoparticles. *Front Microbiol* **6**, 591 (2015).
52. Zhang, T. C. & Bishop, P. L. Density, porosity and pore structure of biofilms. *Water Res* **28**, 2267-2277 (1994).
53. Rosenthal, A. F. et al. Morphological analysis of pore size and connectivity in a thick mixed culture biofilm. *Biotechnol Bioeng* **115**, 2268-2279 (2018).
54. Chew, S. C. et al. Dynamic remodeling of microbial biofilms by functionally distinct exopolysaccharides. *MBio* **5**, e01536-14 (2014).
55. Forier, K. et al. Transport of nanoparticles in cystic fibrosis sputum and bacterial biofilms by single-particle microscopy. *Nanomedicine* **8**, 935-949 (2013).
56. Peulen, T. O. & Wilkinson, K. J. Diffusion of nanoparticles in a biofilm. *Environ Sci Technol* **45**, 3367–3373 (2011).
57. Abdulkarim, M. et al. Nanoparticle diffusion within intestinal mucus: Three-dimensional response analysis dissecting the impact of particle surface charge,

size and heterogeneity across polyelectrolyte, pegylated and viral particles. *Eur J Pharm Biopharm* **97**, 230–238 (2015).

58. Sahle-Demessie, E. & Tadesse, H. Kinetics and equilibrium adsorption of nano-TiO_2 particles on synthetic biofilm. *Surf Sci* **60**, 1177–1184 (2011).
59. Zijnge, V. et al. Oral Biofilm Architecture on Natural Teeth. *PLoS ONE* **5**, e9321 (2010).
60. Bjarnsholt, T. et al. Why chronic wounds will not heal: a novel hypothesis. Wound Repair Regen **16**, 2–10 (2008).
61. Donlan, R. M. & Costerton, J. W. Biofilms: Survival mechanisms of clinically relevant microorganisms. *Clin Microbial Rev* **15**, 167-193 (2002).
62. Peterson, B. W. et al. Viscoelasticity of biofilms and their recalcitrance to mechanical and chemical challenges. *FEMS Microbiol Rev* **39**, 234-245 (2015).
63. Rogers, S. S., van der Walle, C. & Waigh, T. A. Microrheology of bacterial biofilms *in vitro*: *Staphylococcus aureus* and *Pseudomonas aeruginosa*. *Langmuir* **24**, 13549-13555 (2008).
64. Lebeaux, D., Ghigo, J-M. & Beloin, C. Biofilm-related infections: bridging the gap between clinical management and fundamental aspects of recalcitrance toward antibiotics. *Microbiol Mol Biol Rev* **78**, 510–543 (2014).
65. Huang, J. X. et al. Mucin binding reduces colistin antimicrobial activity. *Antimicrob Agents Chemother* **59**, 5925-5931 (2015).
66. Walters, M. C. 3rd., Roe, F., Bugnicourt, A., Franklin, M. J. & Stewart, P. S. Contributions of antibiotic penetration, oxygen limitation, and low metabolic

639 activity to tolerance of *Pseudomonas aeruginosa* biofilms to ciprofloxacin and
640 tobramycin. *Antimicrob Agents Chemother* **47**, 317–323 (2003).
641 67. Percival, S. L., Hill, K. E., Malic, S., Thomas, D. W. & Williams, D. W.
642 Antimicrobial tolerance and the significance of persister cells in recalcitrant
643 chronic wound biofilms. *Wound Repair Regen* **19**, 1–9 (2011).
644 68. Zrelli, K. et al. Bacterial biofilm mechanical properties persist upon antibiotic
645 treatment and survive cell death. *New J Phys* **15**, 125026 (2013).
646 69. Klinger-Strobel, M., Stein, C., Forstner, C., Makarewicz, O. & Pletz, M. W.
647 Effects of colistin on biofilm matrices of *Escherichia coli* and *Staphylococcus*
648 *aureus*. *Int J Antimicrob Agents* **49**, 471-479 (2017).
649 70. EUCAST. Breakpoint tables for interpretation of MICs and zone diameters.
650 Clinical Breakpoints for Bacteria (2018). Available at:
651 http://www.eucast.org/fileadmin/src/media/PDFs/EUCAST_files/Breakpoint_tab
652 les/v_8.1_Breakpoint_Tables.pdf (Accessed: 26 March 2020).
653 71. Yang, Q. E. et al. Compensatory mutations modulate the competitiveness and
654 dynamics of plasmid-mediated resistance in *Escherichia coli* clones. *ISME J* **14**,
655 861-865 (2020).
656 72. Geddes-McAlister, J., Kugadas, A., Gadjeva, M. Tasked with a challenging
657 objective: Why do neutrophils fail to battle *Pseudomonas aeruginosa* biofilms.
658 *Pathogens* **8**, 283.
659 73. Connaughton, A., Childs, A., Dylewski, S., Sabesan V. J. Biofilm disrupting
660 technology for orthopedic implants: what's on the horizon? *Front Med* **1**, 22
661 (2014).

74. Powell, L. C. et al. Targeted disruption of the extracellular polymeric network of *Pseudomonas aeruginosa* biofilms by alginate oligosaccharides. *NPJ Biofilms Microbiomes* **4**, 13 (2018).
75. Howell-Jones, R. S. Antibiotic use in the treatment of chronic wounds. PhD Thesis, Cardiff University (2007). Available at https://orca.cf.ac.uk/55708/1/U584227.pdf (Accessed: 26 March 2020).
76. Yang, Q. E. et al. Environmental dissemination of *mcr-1* positive Enterobacteriaceae by *Chrysomya* spp. (common blowfly): An increasing public health risk. *Environ Int* **122**, 281-290 (2018).
77. Bonengel, S. et al. Impact of different hydrophobic ion pairs of octreotide on its oral bioavailability in pigs. *J Control Release* **273**, 21-29 (2018).
78. Rohrer, J. et al. Mucus permeating thiolated self-emulsifying drug delivery systems. *Eur J Pharm Biopharm* **98**, 90–97 (2016).
79. Schuster, B. S., Suk, J. S., Woodworth, G. F. & Hanes, J. Nanoparticle diffusion in respiratory mucus from humans without lung disease. *Biomaterials* **34**, 3439–3446 (2013).
80. Birjiniuk, A. et al. Single particle tracking reveals spatial and dynamic organization of the *Escherichia coli* biofilm matrix. *New J Phys* **16**, 085014 (2014).

FIGURE LEGENDS

685 **Figure 1: Heterogeneity of NP movement through *P. aeruginosa* PAO1 and *S. aureus***
686 **1004A (MRSA) biofilm structures.** Heterogeneity of 40, 100, 200 and 500 nm
687 negatively-charged carboxylate modified *Fluo*Spheres® NPs movement through *P.*
688 *aeruginosa* and *S. aureus* biofilms. For each particle type, the effective diffusion
689 coefficient ‹Deff› was calculated for 360 individual particles (n=3 for biofilm
690 experiments, each comprised of 120 particles) over a time interval of 20 sec and then data
691 was ranked into percentiles from the 90th through to 10th percentile. (a and e) negatively-
692 charged 40 nm carboxylate modified *Fluo*Sphere® in *P. aeruginosa* and *S. aureus*
693 biofilms respectively; (b and f) negatively-charged 100 nm carboxylate modified
694 *Fluo*Sphere® in *P. aeruginosa* and *S. aureus* biofilms respectively; (c and g) negatively-
695 charged 200 nm carboxylate modified *Fluo*Sphere® in *P. aeruginosa* and *S. aureus*
696 biofilms respectively; (d and h) negatively-charged 500 nm carboxylate modified
697 *Fluo*Sphere® in *P. aeruginosa* and *S. aureus* biofilms respectively. Fold difference in the
698 figure indicates the fold difference between the 90th and 10th percentiles.
699
700 **Figure 2: Exponential anomalous values ‹α› of *P. aeruginosa* PAO1 and *S. aureus***
701 **(MRSA) biofilms.** Exponential anomalous values ‹α› of (a) *P. aeruginosa* and (b) *S.*
702 *aureus* biofilms using 40, 100, 200 and 500 nm negatively-charged carboxylate modified
703 *Fluo*Spheres®. α is measured based on the relation between the ensemble mean square
704 displacement (MSD) versus time scale of the traced *Fluo*Sphere® particles and reflects
705 the micro-rheological degree of resistance of the biofilm towards traced particles where;
706 $\alpha > 0.5$ indicates viscous resistance; $\alpha < 0.5$ indicates elastic resistance. <MSD>
707 represents the geometric mean of MSDs of 360 particles (n=3, each 120 particles).

Figure 3: Nanoparticle diffusion within and disruption of *E. coli* IR57 (PMB^{Sens}) biofilms treated with Polymyxin B. Polymyxin B (PMB)-treated (2, 8, 16, 32, 64 µg/ml) and untreated PMB^{Sens} *E. coli* IR57 biofilms showing: (a) CLSM 3D and side-on imaging of biofilms grown for 48 h followed by polymyxin B treatment for a further 24 h at 37^{o}C in MH broth, visualized using Syto9® staining (Scale bar, 40 µm; n=3). (b) Diffusion coefficient <Deff> of 100, 200 and 500 nm negatively-charged carboxylate modified *Fluo*Sphere® particles in non-treated versus polymyxin B treated biofilms (n=3, ±SEM). *indicates *Fluo*Sphere® particle sizes of 100, 200 and 500 nm.

Figure 4: Exponential anomalous values ‹α› of *E. coli* IR57 (PMB^{Sens}) biofilms treated with Polymyxin B. Exponential anomalous values ‹α› of *E. coli* biofilms in response to polymyxin B treatment using 100, 200 and 500 nm negatively-charged carboxylate *Fluo*Spheres® (a) untreated control; (b) 2; (c), 8; (d), 16; (e), 32; and (f) 64 µg/ml polymyxin B treatment. α is measured based on the relation between the ensemble mean square displacement (MSD) versus time scale of the traced *Fluo*Sphere® particles and reflects the micro-rheological degree of resistance of the biofilm towards traced particles where; $\alpha > 0.5$ indicates viscous resistance; $\alpha < 0.5$ indicates elastic resistance. <MSD> represents the geometric mean of MSDs of 360 particles (n=3, each 120 particles).

Figure 5: Creep Compliance of *E. coli* IR57 biofilms treated with Polymyxin B.

Creep compliance (J(T)) of *E. coli* IR57 (PMB^{Sens}) biofilms (measured using the ensemble mean square displacement <MSD> versus lag time of 100, 200 and 500 nm negatively-charged carboxylate modified *Fluo*Sphere® particles) representing biofilm deformation in response to polymyxin B treatment (2, 8, 16, 32 and 64 μg/ml) versus untreated biofilm. (a) Untreated *E.coli* biofilms for 100, 200 and 500 nm *Fluo*Sphere® particles and (b) 100 nm *Fluo*Sphere® particles, (c) 200 nm *Fluo*Sphere® particles (d) 500 nm *Fluo*Sphere® particles, in response to polymyxin B treatment.

Figure 6: Heterogeneity of NP movement through PMB^{Sens} *E. coli* IR57 and PMB^{R} *E. coli* PN47 biofilm structures +/- Polymyxin B treatment. Heterogeneity of 200 nm negatively-charged carboxylate modified *Fluo*Spheres® movement within *E. coli* biofilms. Untreated controls (a) PMB^{Sens} *E. coli* IR57, (b) PMB^{R} *E. coli* PN47. Polymyxin B- (PMB; 8 μg/ml) treated biofilms (c) PMB^{sens} *E. coli* IR57, (d) PMB^{R} *E. coli* PN47. For each particle type, the effective diffusion coefficient ‹Deff› was calculated for 360 individual particles (n=3 for biofilm experiments, each comprised of 120 particles) over a time interval of 20 sec and the data ranked into percentiles (90^{th} to 10^{th}). Fold difference in the figure indicates the fold difference between the 90th and 10th percentiles.

Figure 7: Creep compliance of PMB^{Sens} *E. coli* IR57 and PMB^{R} *E. coli* PN47 biofilm structures +/- Polymyxin B treatment. Creep compliance (J(T)) of polymyxin B (PMB,

8 μg/ml) treated (dashed lines) and untreated control (solid lines) *E. coli* IR57 and PN47 biofilms (measured using ensemble mean square displacement <MSD> versus time of 200 nm negatively-charged carboxylate modified *Fluo*Sphere® particles) .

Supplementary Figure 1: Comparison of *P. aeruginosa* and *S. aureus* biofilm structures. CLSM 3D imaging of (a) *P. aeruginosa* PAO1 and (b) *S. aureus* 1004A (MRSA) biofilms grown for 72 h at 37°C in MH broth, using Syto9® staining (Scale bar, 40 μm; n=3).

Table 1. NP diffusion within *P. aeruginosa* PAO1 and MRSA biofilm structures. Diffusion coefficients of 40, 100, 200 and 500 nm negatively charged carboxylate modified *Fluo*Spheres® and positively-charged amine modified *Fluo*Spheres® in water calculated by Stoke-Einstein equation versus their effective diffusion coefficients through *P. aeruginosa* PAO1 and *S. aureus* (MRSA) biofilms measured by the MPT technique.

Table 2. NP diffusion within PMB^R and PMB^{sens} *E. coli* biofilms +/- polymyxin B treatment. Diffusion coefficients <Deff> of 200 nm negatively charged carboxylate modified *Fluo*Spheres® in water (calculated by Stoke-Einstein equation) versus their effective diffusion coefficients (measured by MPT) through PMB^R and PMB^{sens} *E. coli* biofilms with/without polymyxin B treatment (8 μg/ml).

Table 1. NP diffusion within *P. aeruginosa* PAO1 and MRSA biofilm structures. Diffusion coefficients of 40, 100, 200 and 500 nm negatively charged carboxylate modified *Fluo*Spheres® and positively-charged amine modified *Fluo*Spheres® in water calculated by Stoke-Einstein equation versus their effective diffusion coefficients through *P. aeruginosa* PAO1 and *S. aureus* (MRSA) biofilms measured by the MPT technique.

*Fluo*Sphere®	*Fluo*Sphere® size (nm) Mean (PDI)	*Fluo*Sphere® zeta potential (mV) Mean (±SEM)	Diffusion coefficient in water (D°) (cm^2/s x10^{-9})	Diffusion coefficient $<Deff>_{PAO1}$ (cm^2/s x10^{-9}) Mean (±SEM)	% ratio $<Deff>_{PAO1}$ /D°	Diffusion coefficient $<Deff>_{MRSA}$ (cm^2/s x10^{-9}) Mean (± SEM)	% ratio $<Deff>_{MRSA}$ /D°
-ve carboxylate	54.73 (0.08)	-37.86 (±0.85)	82.11	3.1493 (±0.6071)	3.8352	1.1584 (±0.1945)	1.4107
-ve carboxylate	108.9 (0.026)	-40.96 (±2.05)	41.27	1.6647 (±0.3695)	4.0338	0.3549 (±0.0624)	0.8600
-ve carboxylate	239.4 (0.031)	-40.83 (±1.30)	18.77	0.0358 (±0.0067)	0.1907	0.0031 (±0.0006)	0.0165
-ve carboxylate	517.2 (0.059)	-40.83 (±2.07)	8.69	0.0165 (±0.0038)	0.1899	0.0038 (±0.0007)	0.0437
+ve amine	204.2 (0.029)	+8.90 (±0.53)	22.01	0.0061 (±0.0015)	0.0277	0.0074 (±0.0017)	0.0336

$<Deff>_{PAO1}$ and $<Deff>_{MRSA}$ indicate <Deff> in *P. aeruginosa* PAO1 and *S. aureus* MRSA biofilms respectively.
PDI, polydispersity index.
± represents standard error of the mean (SEM; n=3).

1

Table 2. NP diffusion within PMB^R and PMB^{sens} *E. coli* biofilms +/- polymyxin B treatment. Diffusion coefficients <Deff> of 200 nm negatively charged carboxylate modified *Fluo*Spheres® in water (calculated by Stoke-Einstein equation) versus their effective diffusion coefficients (measured by MPT) through PMB^R and PMB^{sens} *E. coli* biofilms with/without polymyxin B treatment (8 µg/ml).

E. coli strain	Polymyxin B treatment (8 µg ml^{-1})	Diffusion coefficient in water (D°) ($cm^2/s \times 10^{-9}$)	Diffusion coefficient $<Deff>_{E.\ coli}$ ($cm^2/s \times 10^{-9}$) Mean (± SEM)	% ratio <Deff>/D°
PMB^{sens} IR57	-	18.77	0.0643 (±0.0158)	0.3426
	+	18.77	0.3400 (±0.0805)	1.8114
PMB^R PN47	-	18.77	0.0198 (±0.0038)	0.1055
	+	18.77	0.0137 (±0.0025)	0.0730

$<Deff>_{E.\ coli}$ indicates <Deff> in PMB^R and PMB^{sens} *E. coli* biofilms.
± represents standard error of the mean (SEM; n=3).

Fig. 1

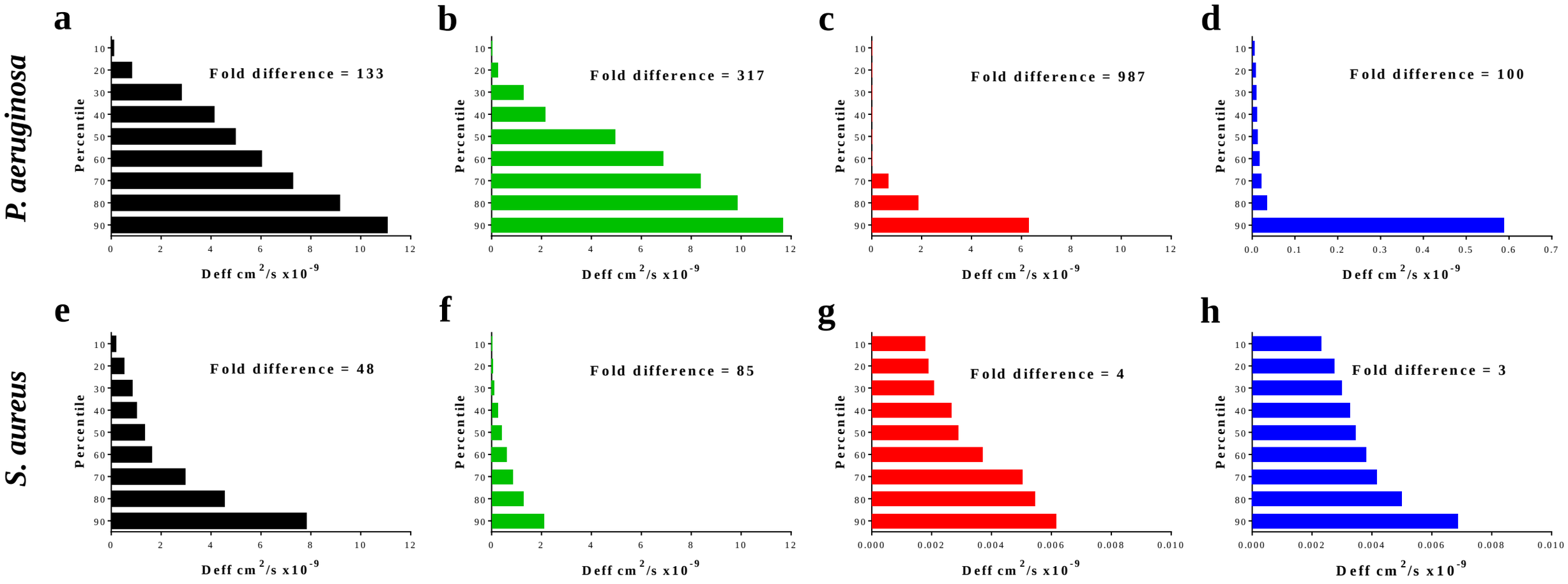
P. aeruginosa
S. aureus
a
b
c
d
e
f
g
h
Fold difference = 133
Fold difference = 317
Fold difference = 987
Fold difference = 100
Fold difference = 48
Fold difference = 85
Fold difference = 4
Fold difference = 3
Percentile
Deff cm 2/s x10-9

Fig. 2

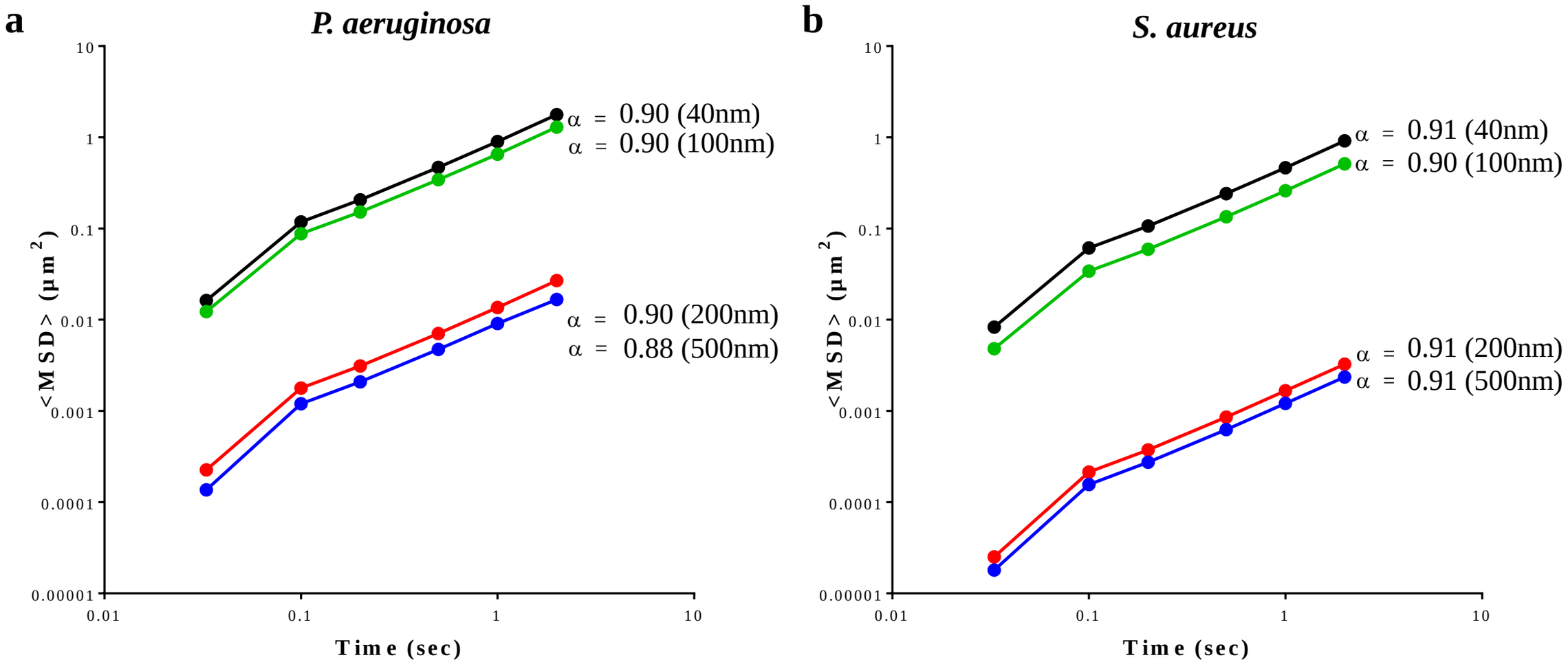
a
P. aeruginosa
b
S. aureus
<MSD> (μm²)
Time (sec)
α = 0.90 (40nm)
α = 0.90 (100nm)
α = 0.90 (200nm)
α = 0.88 (500nm)
α = 0.91 (40nm)
α = 0.90 (100nm)
α = 0.91 (200nm)
α = 0.91 (500nm)
10
1
0.1
0.01
0.001
0.0001
0.00001
0.01
0.1
1
10

Fig. 3

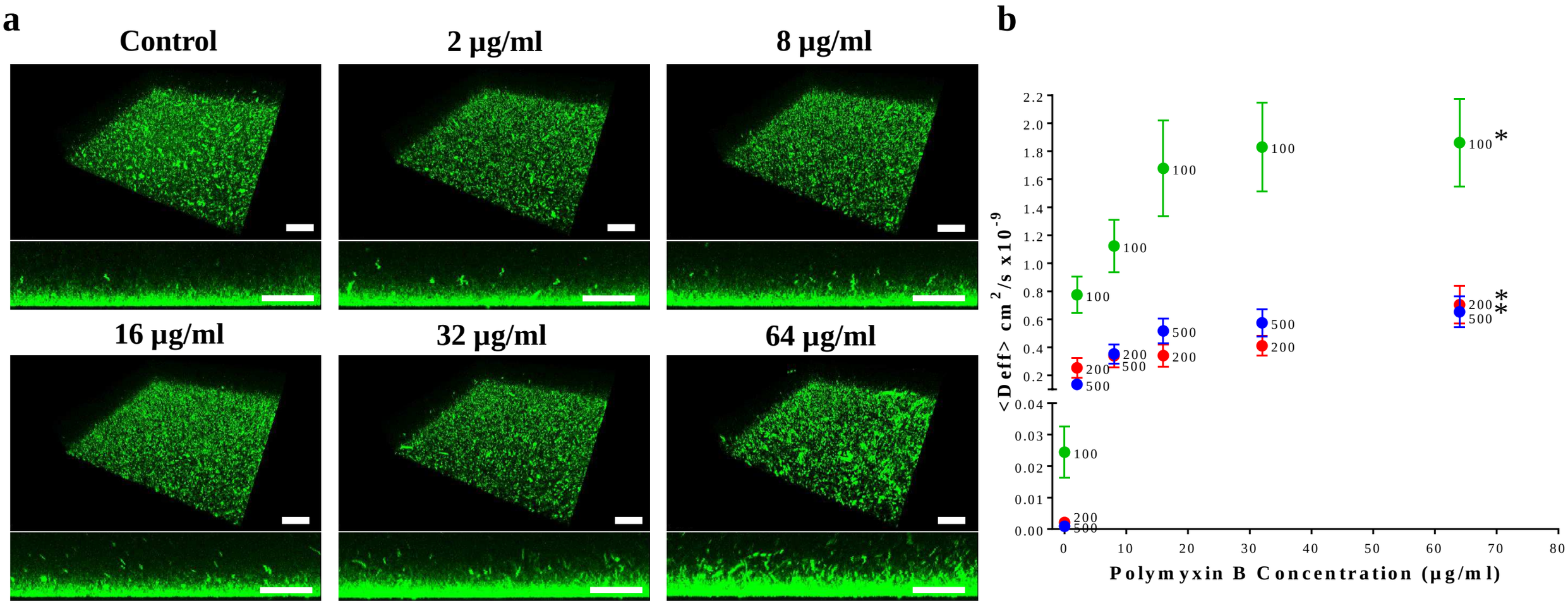
a
Control
2 µg/ml
8 µg/ml
16 µg/ml
32 µg/ml
64 µg/ml
b
<Deff> cm 2/s x10-9
Polymyxin B Concentration (µg/ml)
100
200
500
*
**

Fig. 4

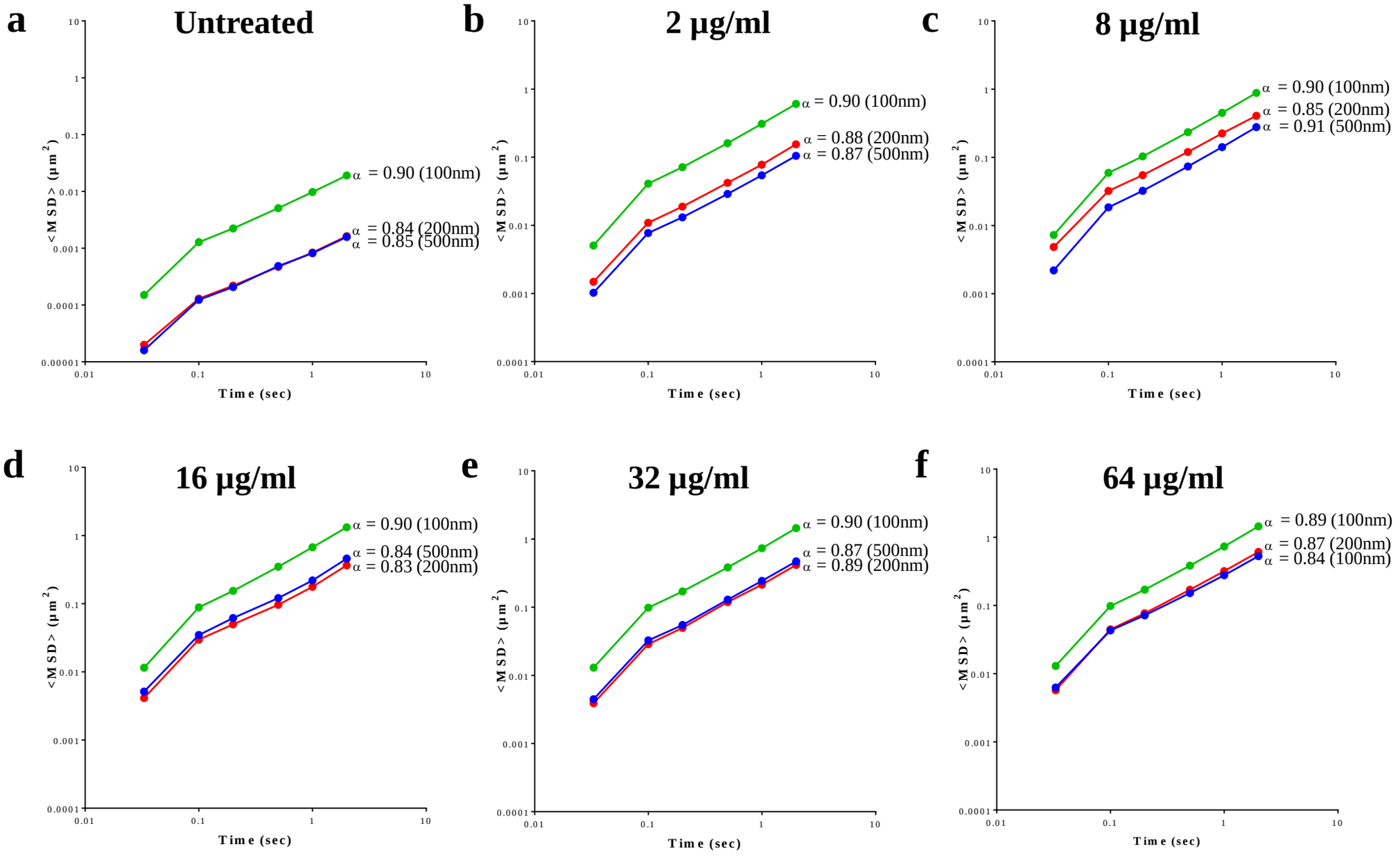
a
Untreated
α = 0.90 (100nm)
α = 0.84 (200nm)
α = 0.85 (500nm)
b
2 μg/ml
α = 0.90 (100nm)
α = 0.88 (200nm)
α = 0.87 (500nm)
c
8 μg/ml
α = 0.90 (100nm)
α = 0.85 (200nm)
α = 0.91 (500nm)
d
16 μg/ml
α = 0.90 (100nm)
α = 0.84 (500nm)
α = 0.83 (200nm)
e
32 μg/ml
α = 0.90 (100nm)
α = 0.87 (500nm)
α = 0.89 (200nm)
f
64 μg/ml
α = 0.89 (100nm)
α = 0.87 (200nm)
α = 0.84 (100nm)
<MSD> (μm²)
Time (sec)

Fig. 5

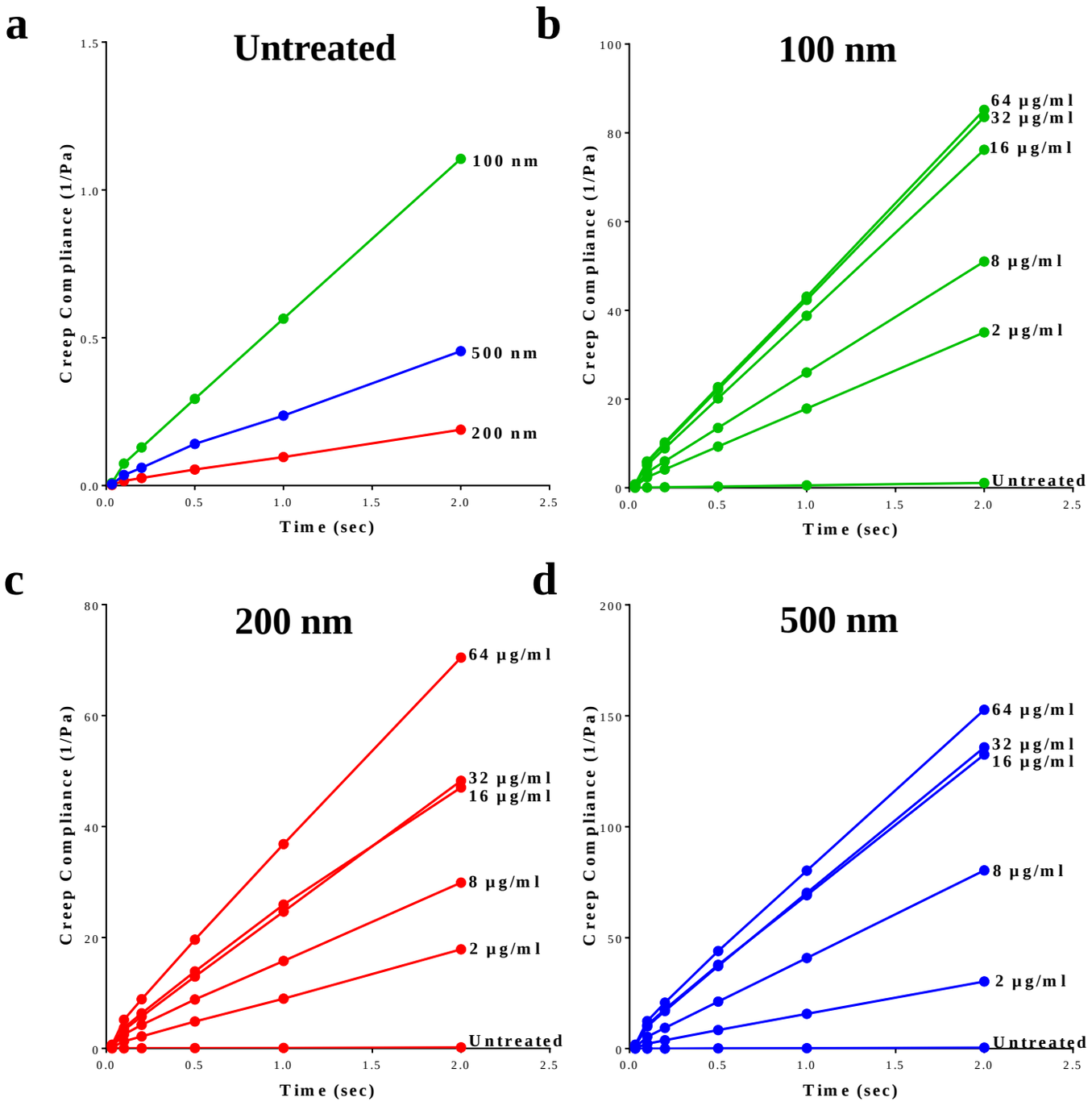
a
Untreated
Creep Compliance (1/Pa)
Time (sec)
100 nm
500 nm
200 nm
b
100 nm
64 µg/ml
32 µg/ml
16 µg/ml
8 µg/ml
2 µg/ml
Untreated
c
200 nm
d
500 nm

Fig. 6

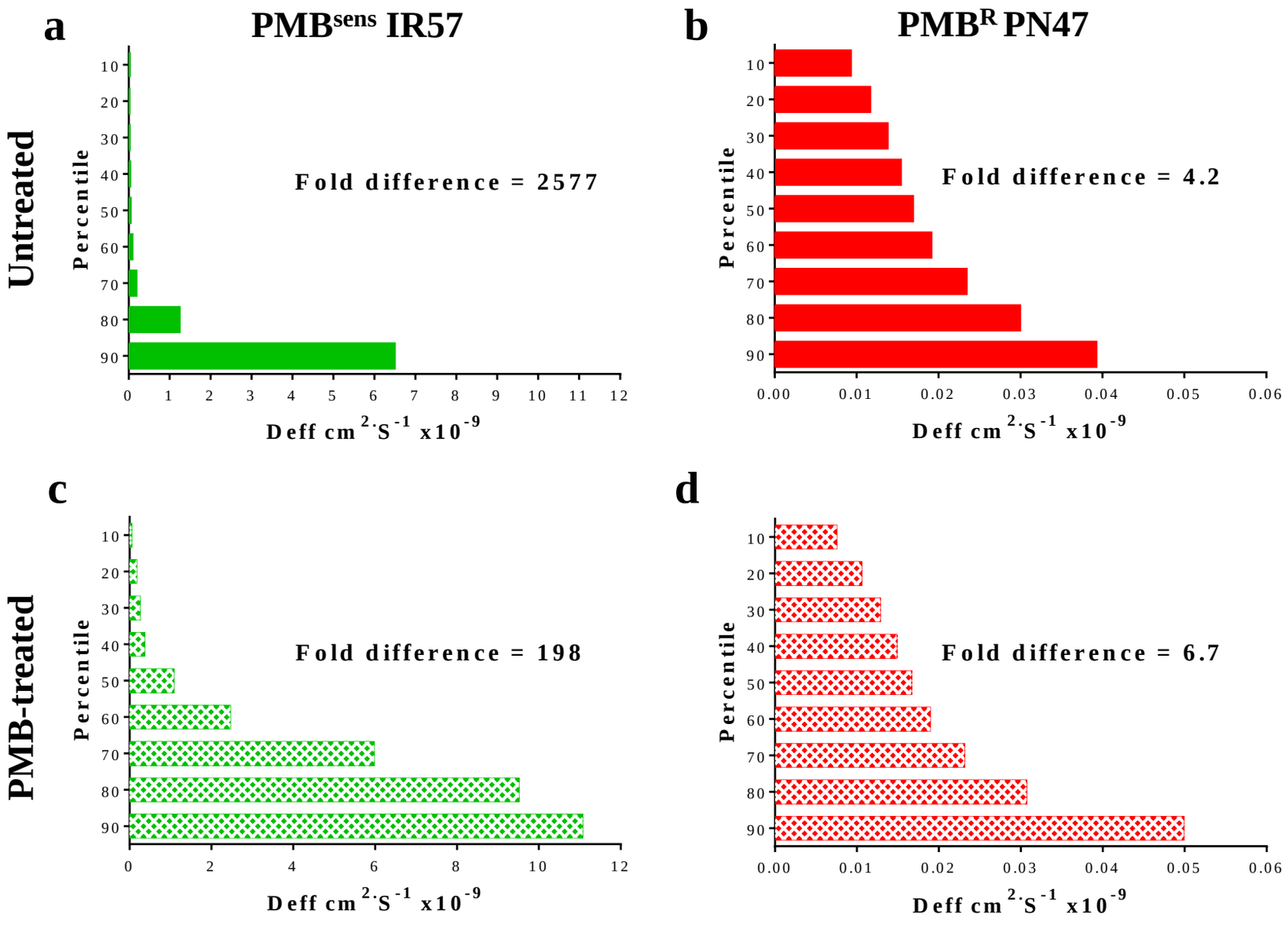
a
PMB^sens IR57
Untreated
Percentile
Fold difference = 2577
Deff cm²·S⁻¹ x10⁻⁹
b
PMB^R PN47
Fold difference = 4.2
Deff cm²·S⁻¹ x10⁻⁹
c
PMB-treated
Percentile
Fold difference = 198
Deff cm²·S⁻¹ x10⁻⁹
d
Fold difference = 6.7
Deff cm²·S⁻¹ x10⁻⁹

Fig. 7

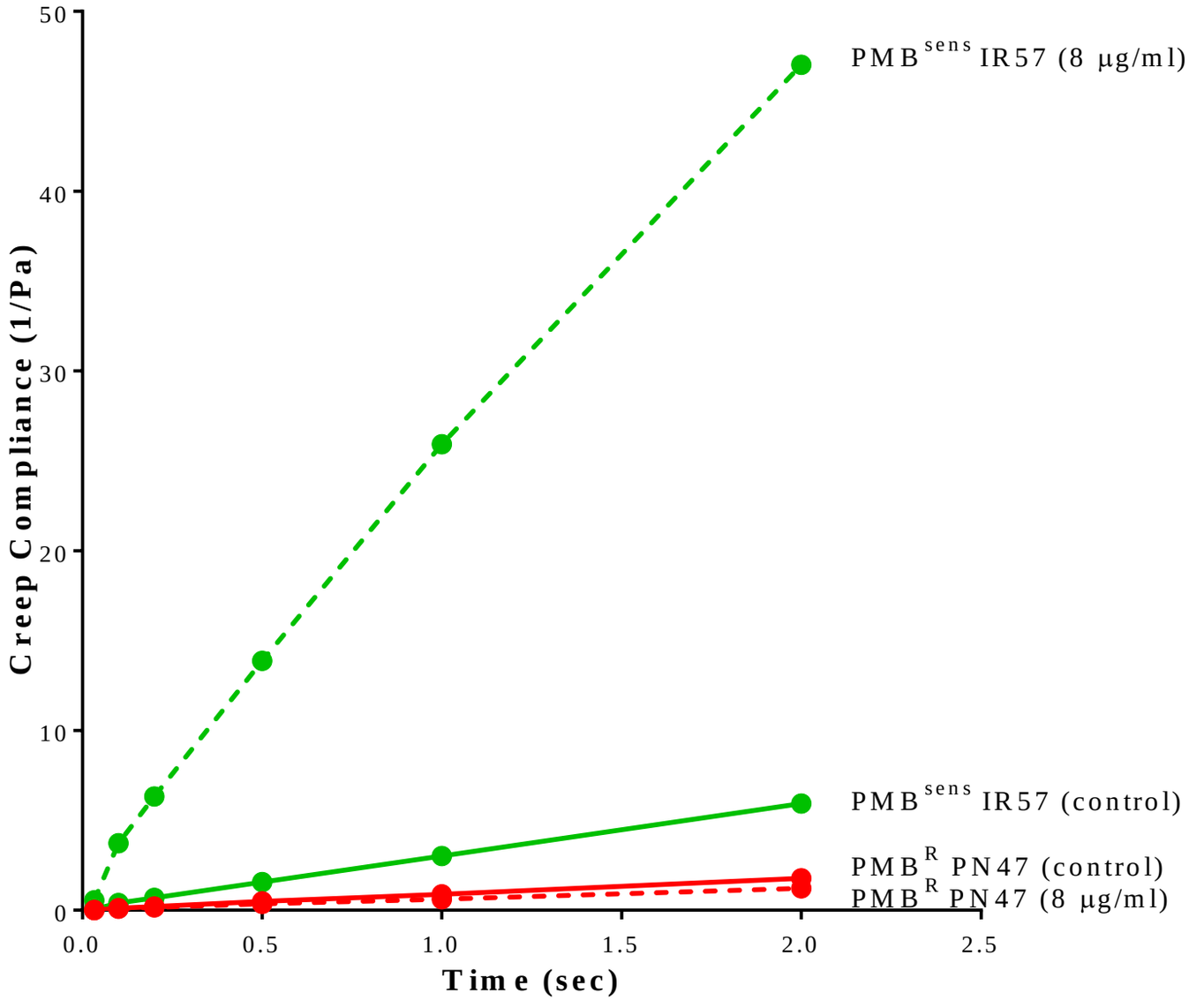
50
40
30
20
10
0
Creep Compliance (1/Pa)
0.0
0.5
1.0
1.5
2.0
2.5
Time (sec)
PMB sens IR57 (8 µg/ml)
PMB sens IR57 (control)
PMB R PN47 (control)
PMB R PN47 (8 µg/ml)